Check for updates

ENGINEERING

Shape and topology morphing of closed surfaces integrating origami and kirigami

Xiangxin Dang, Shujia Chen, Ali Elias Acha, Lei Wu, Damiano Pasini*

Copyright © 2025 The Authors, some rights reserved; exclusive licensee American Association for the Advancement of Science. No claim to original U.S. Government Works. Distributed under a Creative Commons Attribution NonCommercial License 4.0 (CC BY-NC).

A closed surface is generally more resistant to deformation and shape changes than an open surface. An empty closed box, for example, is stiffer and more stable than when it is open. The presence of an opening makes it less constrained, more deformable, and easier to morph, as demonstrated by several studies on open-surface morphing across patterns, materials, and scales. Here, we present a platform to morph closed surfaces with bistability that harnesses a balanced integration of origami and kirigami principles. By harmonizing panel rotation around creases nearly tangent to the closed surface and panel rotation around hinges nearly perpendicular to the closed surface, we show that origami-kirigami assemblages can shape-morph between a cube and a sphere, scale between spheres of dissimilar size, and change topology between a sphere and a torus, with programmed bistability. The framework offers a promising strategy for designing bistable reconfigurable structures and metamaterials with enclosed configurations.

INTRODUCTION

Shape morphing, the ability of an object to change shape in response to an external stimulus or control input (*1*, *2*), is commonly observed in natural organisms to achieve various functionalities. Likewise, in the synthetic world, shape morphing is pursued for the design of shape-shifting materials and multifunctional structures, such as hydrogels (*2*), shape memory alloys (*3*), living composites (*4*), liquid crystal elastomers (*5*), architected dielectric elastomers (*6*), and origami/kirigami structures (*7*). One of their common traits stems from their morphable attributes arising from either the base material or/and the material architecture, both contributing to delivering reconfigurability, large dimensional changes, foldability, and other morphing-driven functionalities. Previous research has so far focused on the transformation of shapes either from a flat state to a curved shape (*8*–*11*) or between distinct curved shapes (*12*, *13*). These transformations are all characterized by open surfaces while morphing from an open surface to a closed surface has also been reported (*14*, *15*). Morphing between closed surfaces, however, is now unexplored, yet it bears large scientific implications and practical applications, as described below.

In topology, a closed surface is a two-dimensional (2D) manifold that has no infinitely distant points and has no boundary (*16*). Typical closed surfaces include the sphere and the torus, which are orientable in the 3D space with distinguishable interior and exterior surfaces forming two-sided surfaces, and the non-orientable Klein bottle, which, on the other hand, is one-sided (*17*). In contrast, while not typically considered a standard mathematical term, open surface in physics often refers to a surface with a defined boundary (*18*), such as a spherical cap (with one boundary) and cylindrical surface (with two boundaries). Closed surfaces have intrinsic characteristics that can offer advantages over open surfaces in various aspects. On the geometric front, for instance, the existence of a boundary implies that an open surface cannot seal off a volume, while an orientable closed surface can break the 3D space into separate regions, an interior, and an exterior. On the mechanics front, a closed surface provides structural stiffness and stability by distributing internal forces more uniformly over the entire geometry. A typical example is the "shear flow" in the closed cross section of a tube, which can resist torsion much more effectively than its counterpart shear flow in an open cross section (*19*). On the application front, a closed surface can encapsulate contents within its volume, offering protection against external factors such as contaminants, radiation, or physical impact. The ability to model and predict the morphing of closed surfaces would enable the optimization of both structural and protective properties, benefiting a diverse range of applications involving, for example, controlled release of drugs (*20*), selective electromagnetic shielding (*21*), and responsive soft robotics (*22*). Despite the benefits summarized above, morphing a closed surface appears more challenging than morphing an open surface. The main reason can be attributed to geometric characteristics. Intuitively, a closed surface is typically obtained by sewing the free boundaries of several open patches to create an enclosed volume. As a result, generating and controlling morphing in a closed surface requires the synchronous motion and evolution of the constituent patches so as to preserve the proper adjacency between them across the sewed boundaries, a requirement that imposes stricter constraints than morphing open patches separately.

Origami, the art of paper folding, and kirigami, paper cutting, offer elegant solutions for transforming flat sheets into curved open surfaces (*23*). They have been successfully applied to develop multifunctional structures and metamaterials at various length scales (*24*, *25*). Both origami and kirigami rely on patch rotations to govern their morphing kinematics, but in distinct ways. In origami, patch rotation occurs around a crease accommodated in the initial plane of a flat sheet, whereas, in kirigami, the rotation axes are out of the initial plane. Compared to origami, kirigami appears to enable shape changes of higher geometric complexity and have more potential to be performed on originally curved surfaces (*14*, *26*), due to the additional degrees of freedom (DOFs) introduced by their slits. On the other hand, origami is favored in cases where the precise control is required over the entire shape transformation (*27*), whereas kirigami has to seek a trade-off between flexibility and controllability (*28*).

Department of Mechanical Engineering, McGill University, Montreal, H3A 2K6, Canada.
*Corresponding author. Email: damiano.pasini@mcgill.ca

Downloaded from https://www.science.org at Princeton University on April 30, 2025

Here, we harness the advantages of both origami and kirigami principles to tackle the challenging task of morphing closed surfaces and imparting bistability. To pursue a morphing platform with high capacity for geometric variation and low complexity for mechanical control, we propose a class of bistable ori-kiri material assemblages that can approximate distinct closed surfaces in both their compact and deployed configurations. In particular, our goal here is to generate bistable morphing between closed surfaces that are dissimilar in size (Fig. 1A), shape (Fig. 1B), and, unprecedentedly, topology (Fig. 1C). The deployed configuration, despite its open slits, covers a closed surface as an inner space is enclosed and bounded by its panels. These slits are comparable in size to the panels, allowing the panels to span the overall closed shape. Based on this consideration, the slits are regarded as an essential component of the closed surface. The ori-kiri assemblages are geometrically constructed by triangular patches with edge connections and vertex connections (Fig. 1, right column). The geometric distribution of creases (i.e., diagonals) and slits (i.e., outer edges) is designed to preserve the congruence between corresponding panels in their compact and deployed states, with the vertices lying on a given closed surface. The panels can fold around their diagonal hinges (origami principle) and rotate at their vertices connected to the neighbor panels (kirigami principle) and, hence, realize the closed-surface morphing. Mechanically, the diagonal connections are realized by origami hinges that are nearly tangent to the closed surfaces, while the vertex connections are realized by kirigami hinges that are nearly perpendicular to the closed surfaces. The bistable reconfiguration of the ori-kiri assemblages is guided by their origami hinges and kirigami hinges, each allowing 1 DOF. Beyond the bistable material assemblages, we further propose a class of unitary-piece ori-kiri metamaterials with functionalities leveraging shape morphing and topology morphing.

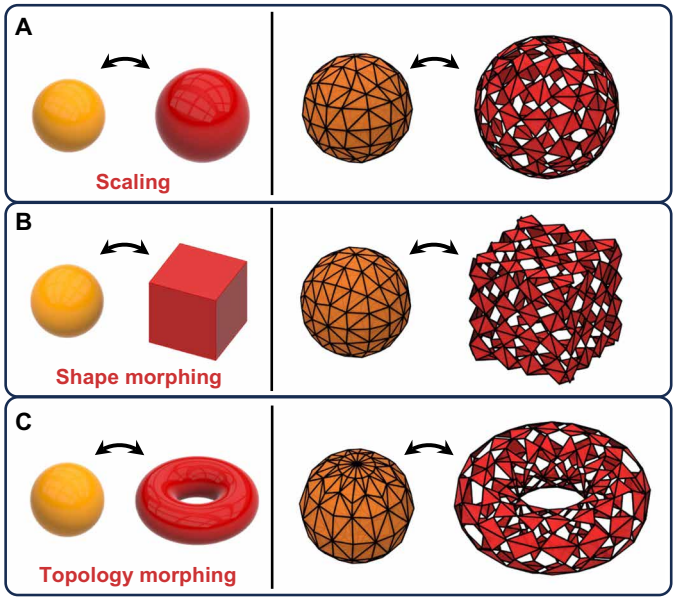

Fig. 1. Three types of closed-surface morphing (left column) and their conceptual realizations with ori-kiri assemblages (right column). (**A**) Scaling between spheres of dissimilar radius. (**B**) Shape morphing between sphere and cube. (**C**) Topology morphing between sphere (genus-0) and torus (genus-1).

RESULTS

Design strategy

We implement a two-stage process to design our ori-kiri material assemblages with the dual goal of attaining both geometrical compatibility and mechanical bistability. In the first stage, we treat the kirigami hinges as spherical joints (each with 3 DOFs) and optimize the distribution of the panel vertices of the ori-kiri material assemblages, seeking their geometric compatibility at two closed surfaces. This first stage produces an ori-kiri mechanism with multiple kinematic DOFs. In the second step, we determine the rotation axis of each kirigami hinge and freeze all the kinematic DOFs, such that each mechanism becomes a bistable material assemblage.

As a demonstration, we exemplify our two-stage platform through the shape morphing between a cube and a sphere. The key idea is to build two systems of quadrilateral panels—the vertices of one system on the cube and those of the other on the sphere—with identical number of panels and identical rules of vertex and edge connections (Fig. 2A). To apply the folding principle, each quadrilateral panel is divided into two triangular panels by a selected diagonal. The common edge of the two triangular panels can be seen as the crease of the quadrilateral panel. For the cube, we naturally adopt the regular checkerboard as the initial geometry for its six faces. The vertex connections are prescribed inside each face to make them rotating-square (RS) mechanisms with assigned diagonals and on the intersections of the faces to make them synergistically deployable (text S1 and figs. S1 and S2). We denote this system of triangles with their connections as a RS mesh. The deployed version of the RS mesh is generated by mapping deployed RS patterns onto the sphere (fig. S3). The consistency between the compact and deployed RS meshes is realized by the 2D parametrization of vertex locations on the closed surfaces (text S2 and fig. S4) and the deployment of the rotating squares in the parameter space (text S3 and fig. S5). The map from a planar parameter space to a general curved closed surface does not necessarily preserve sizes and shapes, yet it paves the way for moving the vertices within their surfaces.

Starting from two initial RS meshes, where the identical diagonals and connection rules for neighboring panels are prescribed, our first goal is to pursue congruence between the corresponding panels (i.e., geometrical compatibility) in the compact RS mesh on the cube and deployed RS mesh on the sphere (Fig. 2C). To this end, the first-stage design adopts spherical joints for vertex connections of panels and optimizes panel vertex locations through the following formulation

$$\min_{\mathbf{P}_c,\mathbf{P}_d,a_c} f_{\text{obj.}}\left(\mathbf{P}_d, a_d\right) \quad \text{s. t.} \begin{cases} f_{\text{comp.}}\left(\mathbf{P}_c, \mathbf{P}_d, a_c, a_d, \mathbf{c}\right) = 0 \\ \mathbf{f}_{\text{sym.}}\left(\mathbf{P}_c, \mathbf{P}_d\right) = 0 \\ \mathbf{f}_{\text{pos.}}\left(\mathbf{P}_c, \mathbf{P}_d\right) \le 0 \\ \mathbf{f}_{\text{cont.}}\left(\mathbf{P}_c, \mathbf{P}_d\right) \le 0 \end{cases} \tag{1}$$

where $\mathbf{P}_c$ and $\mathbf{P}_d$ are the set of vertex-location parameters of the compact and deployed RS meshes, respectively (fig. S6); a_c is the size of the compact configuration, equal to the half side length of the cube; a_d is the size of the deployed configuration, equal to the radius of the sphere; and $\mathbf{c}$ is the array of diagonal assignment. For the example in Fig. 2A, the components of $\mathbf{c}$ are given by

$$c_{i,j,k} = \begin{cases} +1, & |i-j| < 2 \\ -1, & |i-j| \ge 2 \end{cases} \tag{2}$$

Downloaded from https://www.science.org at Princeton University on April 30, 2025

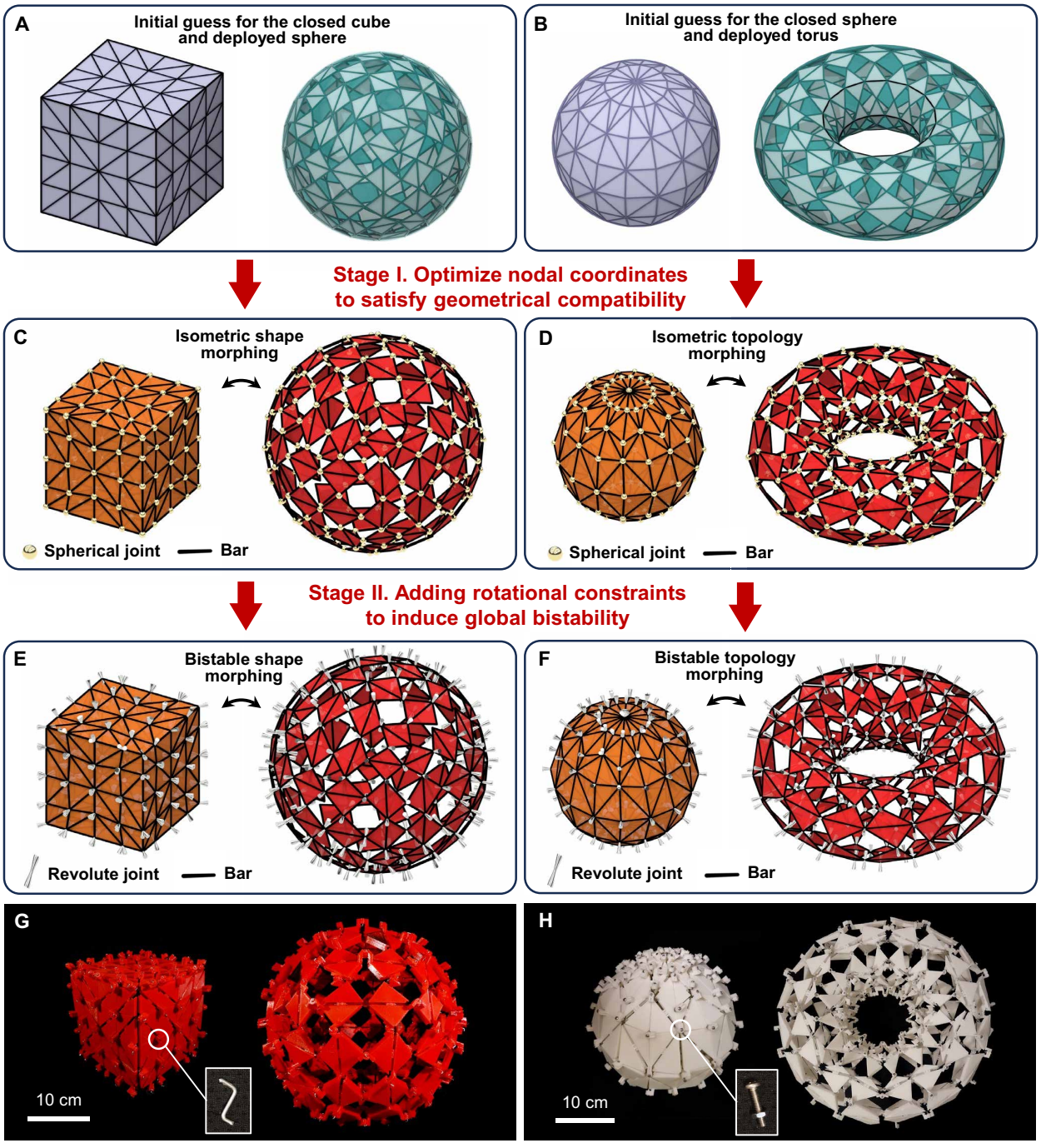

Fig. 2. Two-stage design of bistable ori-kiri assemblages with features of shape morphing and topology morphing. (**A** and **B**) Initial mesh, (**C** and **D**) the first design stage to obtain geometric compatibility, and (**E** and **F**) the second design stage to obtain mechanical bistability for the shape morphing between a cube and a sphere [(A), (C), and (E)] and the topology morphing between a sphere and a torus (B, D, and F). (**G**) 3D printed shape-morphing ori-kiri assemblage: compact cube (left) and deployed sphere (right). Inset: Thin metal rods. (**H**) 3D printed topology-morphing ori-kiri assemblage: compact sphere (left) and deployed torus (right). Inset: Thick screws and nuts.

where the subscripts indicate the quadrilateral on the ith column and jth row of the kth face of the RS mesh, for $i,j = 1,2,3,4$ and $k = 1, 2, \ldots, 6$. The entries $+1$ and -1 represent the major and minor diagonals, respectively, for each quadrilateral composed of two edge-connected triangular panels (fig. S7).

While the detailed formulation of the objective and constraint functions are given in text S4, here, we describe each of them briefly. The objective function $f_{\text{obj.}}$ controls the degree of deployment of the ori-kiri assemblage with a reference opening angle ω (fig. S8). The compatibility constraint function $f_{\text{comp.}}$ controls the isometry of the compact and deployed configurations. To quantify the compatibility, we define the following metric function

$$f_{\text{metric}}(\mathbf{X}_c, \mathbf{X}_d, \mathbf{c}) = \frac{1}{N_e}\sum_{k=1}^{N_e}\left(s_{c,k} - s_{d,k}\right)^2 \quad (3)$$

Downloaded from https://www.science.org at Princeton University on April 30, 2025

where $s_{c,k}$ and $s_{d,k}$ are the kth edge lengths of the compact and deployed configurations, respectively; and $\mathbf{X}_c$ and $\mathbf{X}_d$ are the vertex positions of the compact and deployed configurations, respectively. The summation goes through all the N_e edges. However, f_{metric} cannot be directly used in the optimization formulation because it does not involve the shapes of the target morphing surfaces. The compatibility constraint function $f_{comp.}$ should receive the parameters $\mathbf{P}_c$ and $\mathbf{P}_d$ and the size variables a_c and a_d as input instead of the vertex positions $\mathbf{X}_c$ and $\mathbf{X}_d$. To this end, we define the constraint function for compatibility as

$$f_{comp.}(\mathbf{P}_c, \mathbf{P}_d, a_c, a_d, \mathbf{c}) = f_{metric}\left[\mathbf{X}_c(\mathbf{P}_c; a_c), \mathbf{X}_d(\mathbf{P}_d; a_d), \mathbf{c}\right] / \ell_d^2 \quad (4)$$

The characteristic length ℓ_d is determined by the size of the deployed configuration. Specifically, the deployed sphere of radius a_d defines $\ell_d = 2\pi a_d / N$. For the compact cube, the map $\mathbf{X}_c(\mathbf{P}_c; a_c)$ is expressed by

$$(x, y, z) = \mathbf{g}_{cube-RS}(p, q; k, a_c);\ (x, y, z) \in \mathbf{X}_c,\ (p, q) \in \mathbf{P}_c,\ k = 1, 2, \ldots, 6 \quad (5)$$

For the deployed sphere, the map $\mathbf{X}_d(\mathbf{P}_d; a_d)$ is expressed by

$$(x, y, z) = \mathbf{g}_{sphere-RS}(p, q; k, a_d);\ (x, y, z) \in \mathbf{X}_d,\ (p, q) \in \mathbf{P}_d,\ k = 1, 2, \ldots, 6 \quad (6)$$

It is worth noting that the index k denotes the six different faces on the RS meshes. The explicit expressions of the functions $\mathbf{g}_{cube-RS}$ and $\mathbf{g}_{sphere-RS}$ are given in text S2. In addition to $f_{comp.}$, we have some other constraint functions that confine the vertex distributions on the ori-kiri assemblages. The symmetry constraint function $\mathbf{f}_{sym.}$ applies three orthogonal planes of mirror symmetry to the compact and deployed RS meshes with the goal of providing a better regularity of the panels in the optimized RS meshes. The position constraint function $\mathbf{f}_{pos.}$ restricts the relative positions of vertices to avoid distortion of the optimized RS meshes, including non-convexity of panels, intersection of edges, and orientation reversal of panels (fig. S9). The continuity constraint function $\mathbf{f}_{cont.}$ aligns the corresponding vertices and removes the redundant slits on the intersections where the six faces meet with each other (fig. S10).

We use the sequential quadratic programming (SQP) algorithm to solve the optimization problem in Eq. 1. To obtain the optimized ori-kiri assemblage in Fig. 2C, we prescribe the radius of the deployed sphere as $a_d = 1$; the initial side length of the compact cube is specified as $2a_c = \sqrt{2}$; in the objective function, the reference opening angles are specified to be a constant $\omega = 0.5\pi$ (text S4). By modeling the assemblage with a truss network where the bars represent the panel edges (fig. S11), we can compute the degree of kinematic indeterminacy (DOKI) of the optimized ori-kiri assemblage (text S5). We note that the DOKI is the DOF of a bar-and-hinge system under infinitesimal nodal displacement. In the remaining text, we simply use DOF to refer to DOKI. The analysis shows that the compact cube has 180 DOFs and the deployed sphere has 138 DOFs, a result indicating that the obtained ori-kiri assemblage is kinematically indeterminate (i.e., with multi-DOFs of motion); therefore, from a physics standpoint, it has zero-energy transition paths between its compact and deployed configurations (Fig. 2C). The excessive number of DOFs can cause two undesired issues: first, controlling the transition between the two zero-energy states and, second, maintaining the desired shapes at the zero-energy states. To tackle them, we suppress all the DOFs in the second design stage by replacing the spherical joints with revolute joints, so as to empower the ori-kiri assemblage with kinematic determinacy and bistability.

The second design stage seeks to determine the directions of the revolute joints that guide the transition between the compact and deployed configurations (Fig. 2E). To this end, we calculate the relative rotation matrix for each pair of vertex-connected triangular panels and then calculate the direction of their rotation axis; we also determine the rotation angle from the components of the rotation matrix (text S5). Prior and post the transition (either deploying or undeploying), the resulting orientation of each rotation axis is unchanged with respect to the panels (that shares the axis) as an object of reference (fig. S12). As a result, the revolute joints can guide panel rotation around their axes and panel transition between the compact and deployed configurations. Compared to spherical joints with 3 DOFs, each revolute joint only allows the relative rotation of panels around the rotation axis, which can substantially decrease the DOFs of the ori-kiri assemblage. Adopting the truss model again, where the bars replace the panel edges, we perform the kinematic indeterminacy analysis and find that the hinged ori-kiri assemblage in Fig. 2E has 0 DOF at both the compact and the deployed states (text S5). This result attests that the assemblage has converted to a structure with two zero-energy stable states.

Deployment simulation

The kinematic indeterminacy analysis is carried out on the truss model of bars and hinges (i.e., revolute joints), showing that the ori-kiri assemblage is stable at the states of the compact cube and deployed sphere. To further illustrate the global bistability of the assemblage between its two compatible states, we simulate the deployment path with a simplified energy formulation of the truss model. Basically, we assume the energy is contributed by two sources (fig. S13): the stretching energy of the bars (denoted by E_S) and the off-axial-rotation energy at the hinges (denoted by E_R). We write the stretching energy E_S as

$$E_S(\mathbf{X}) = \frac{1}{2}\sum_{n=1}^{N_{bar}}\left[k_{S,n}\left(s'_n - s_n\right)^2\right] \quad (7)$$

where s_n and s'_n are the original and deformed lengths of the nth bar, respectively; $k_{S,n}$ is the stiffness of the nth bar; $\mathbf{X}$ is the node positions of the truss; and N_{bar} is the total number of bars ($N_{bar} = N_e$).

For each hinge (indexed by m), it would be convenient to formulate the energy if the rotation between two hinged panels can be decomposed into the rotation around the hinge axis (denoted by γ_m) and the rotation around an axis that is perpendicular to the hinge axis (denoted by δ_m). It can be proved that, when the off-axial rotation δ_m and the bar strain $\varepsilon_n = \left(s'_n - s_n\right)/s_n$ are small, this decomposition exists and is unique (text S6). We assume that the rotation γ_m does not consume energy; hence, the rotation energy can be written as

$$E_R(\mathbf{X}) = \frac{1}{2}\sum_{m=1}^{N_{hinge}}\left(k_R\delta_m^2\right) \quad (8)$$

Downloaded from https://www.science.org at Princeton University on April 30, 2025

where k_R is the off-axial rotational stiffness and N_{hinge} is the total number of hinges.

We assume a constant axial rigidity EA for all the bars; thus, $k_{S,n} = EA/s_n$. We introduce a characteristic length ℓ_c to nondimensionalize the deformation energy. Specifically, for the assemblage deployed from a cube to a sphere, we define $\ell_c = a_d$, i.e., the half side length of the compact cube. Then, the scaled stretching energy and rotational energy are expressed by

$$\overline{E}_S(\mathbf{X}) = E_S(\mathbf{X})/(EA\ell_c) \text{ and } \overline{E}_R(\mathbf{X}) = E_R(\mathbf{X})/(EA\ell_c) \quad (9)$$

respectively. Last, we obtain the total scaled energy

$$\overline{E}_T(\mathbf{X}) = \overline{E}_S(\mathbf{X}) + \overline{E}_R(\mathbf{X}) \quad (10)$$

We assume $k_R = c_R EA\ell_c$, where c_R is a coefficient that adjusts the proportion of $\overline{E}_S$ and $\overline{E}_R$ in $\overline{E}_T$. The coefficient can be expressed in terms of the stiffness by $c_R = k_R/(k_{S,n}s_n\ell_c)$.

We can minimize $\overline{E}_T(\mathbf{X})$ to simulate the deployment of the ori-kiri assemblage, obtaining the intermediate configurations as well as the energy landscape at each step of the deployment path. To apply the loading conditions, we select a set of control nodes $\mathbf{x}_{ctrl}$, prescribe their positions upon deployment, and optimize the positions of the other nodes. Specifically, for the assemblage deployed from a cube to a sphere, we select six pairs of nodes that are located at the center of the six faces of the RS mesh (see movie S1). The main reason for this choice is that these nodes travel a relatively long distance compared to the free points so as to effectively monitor each step of the deployment. We refer to text S6 for the detailed formations of the deformation energy, the loading conditions, and the optimization setup.

As a first initial guess, $c_R = 0.1$, so as to obtain small off-axial-rotation angles and low bar strains (fig. S14), which are consistent with our assumption in the formulation of E_R. The simulated energy landscape features an energy barrier with two zero points at both ends (movie S1), confirming the bistability of the hinged ori-kiri assemblage. To validate the analysis and simulation, we 3D printed panels with extruded hollow cylinders whose axes are those of the revolute joints and pinned them together with thin metal rods (Fig. 2G). Upon deployment, this prototype shows a bistable transition between the closed cubic state and the deployed spherical state (movie S2). Last, a noteworthy observation on each revolute joint is that its orientation is prescribed with respect to the local reference of the panel it belongs to. As a result, morphing from a cube to a sphere is accompanied by changes in the origami folding angle and the kirigami opening angle, as opposed to the revolute joint's orientation.

Extension to other morphing categories

The proposed two-stage design strategy is general in the sense that it can be applied to different types of meshes on dissimilar closed surfaces. This advantage allows us to explore morphing between closed surfaces of distinct topologies. For example, we can use the standard UV mesh to discretize a sphere (Fig. 2B, left; text S1; and fig. S1). The mesh is named hereafter "UV mapping," a texture mapping technique that can unwrap images from a 3D model's surface to a 2D surface (*29*). The standard UV mesh is composed of trapezoids in its main part and two clusters of triangles in the polar region. In analogy to the RS meshes, we assign diagonals to activate origami folding deformations with the goal of attaining curvature changes. We define an array of diagonal assignment $\mathbf{c}$ whose components are defined as

$$c_{i,j} = \begin{cases} +1, & \text{even } i+j \\ -1, & \text{odd } i+j \end{cases} \quad (11)$$

where the subscripts indicate the trapezoid on the ith column and jth row of the UV mesh, for $i = 1, 2, \ldots, 16$ and $j = 2, 3, \ldots, 7$. The array $\mathbf{c}$ describes the diagonal assignment for the compact spherical UV mesh in Fig. 2B.

With the 2D parametrization of the sphere, we can deploy the corresponding UV mesh in the parameter space with specified vertex connection rules and map the deployed pattern onto a torus (texts S2 and S3 and figs. S4, S15, and S16). As a result, we obtain a deployed version of UV mesh on a torus. The torus has a hole, namely, genus-1, that is not embedded by the panels, and, thus, it is distinct from the sphere in terms of topology (Fig. 2B, right). Compared to the initial geometry of the shape-morphing assemblage (Fig. 2A), we have changed the shape and topology of the closed surfaces, as well as the type of meshes to set up the topology-morphing problem. Nevertheless, we can still adopt the two-stage design framework, as summarized below.

At the first stage, we solve Eq. 1, optimizing the vertex-location parameters (fig. S17) on the sphere and torus, to achieve geometrical compatibility between the compact and deployed UV meshes. To this end, we need to modify the parametrization of the closed surfaces. For the compact sphere, the map $\mathbf{X}_c(\mathbf{P}_c; a_c)$ becomes

$$(x, y, z) = \mathbf{g}_{\text{sphere-UV}}(p, q; a_c); (x, y, z) \in \mathbf{X}_c, (p, q) \in \mathbf{P}_c \quad (12)$$

For the deployed torus, the map $\mathbf{X}_d(\mathbf{P}_d; \mathbf{a}_d)$ becomes

$$(x, y, z) = \mathbf{g}_{\text{torus-UV}}(p, q; R, r); (x, y, z) \in \mathbf{X}_d, (p, q) \in \mathbf{P}_d, \mathbf{a}_d = (R, r) \quad (13)$$

The explicit expressions of the functions $\mathbf{g}_{\text{sphere-UV}}$ and $\mathbf{g}_{\text{torus-UV}}$ are given in text S2. With reference to Eq. 1, we note that the size of the deployed configuration has become an array $\mathbf{a}_d = (R, r)$, because a torus is determined by both the major radius R and the minor radius r. To obtain the optimized UV meshes in Fig. 2D, we prescribe the major and minor radii as $R = 1$ and $r = 0.5$, respectively. The radius of the compact sphere a_c is assigned the initial value 1. In the objective function, the reference opening angles are specified to be a constant $\omega = 0.4\pi$.

By assigning spherical joints, we obtain an ori-kiri assemblage with a compact spherical configuration and a deployed toric configuration (Fig. 2D). The two configurations are kinematically indeterminate with 138 DOFs and, hence, connected by uncertain deployment paths with zero-energy, as investigated with the kinematic indeterminacy analysis. In the second stage, we obtain the orientation of the revolute joints by calculating the relative rotation matrices for the vertex-connected panels (Fig. 2F). By assigning the revolute joints, we decrease the DOF of the ori-kiri assemblage to zero and make it bistable, an outcome validated through the analysis of its energy landscape (movie S1). To validate the design, we assembled the 3D printed panels with extruded hollow cylinders whose axes are those of the revolute joints (Fig. 2H). We observe that the topology morphing of the sphere bears larger forces at the equator and the poles, causing the fracture of panels in those regions

Downloaded from https://www.science.org at Princeton University on April 30, 2025

upon transition between the two compatible configurations. To tackle this issue, we tune the tightness of the connections, realized with screws and nuts (Fig. 2H, inset). When the bolts are tighter, the contact in the hinges increases, generating a small amount of friction that reduces the mobility of the model. On this front, we emphasize that the bolts are never fully tight; the intention is not to restrict hinge motion completely, rather to tune the hinge stiffness so as to better capture the morphing and appreciate the stable configurations. Two levels of tightness are used. The first one is tighter and allows both the compact sphere and the deployed torus to retain their shapes under external loads (movie S3). The second one, which is slightly looser than the first one, reduces the energy barrier for the transition while avoiding the fracture of the panels (movie S3). This approach enables to reconcile stability and reconfigurability within the assemblage without failing the hinges.

In addition to the shape morphing and topology morphing, we can leverage our framework to achieve also the scaling of closed surfaces. This can be accomplished simply by choosing two surfaces of identical shape but dissimilar size for the compact and deployed configurations, respectively. For example, Fig. 3A shows the scaling between two spheres achieved by the ori-kiri assemblage with RS meshes. In addition, by changing the sphere to a cube for the

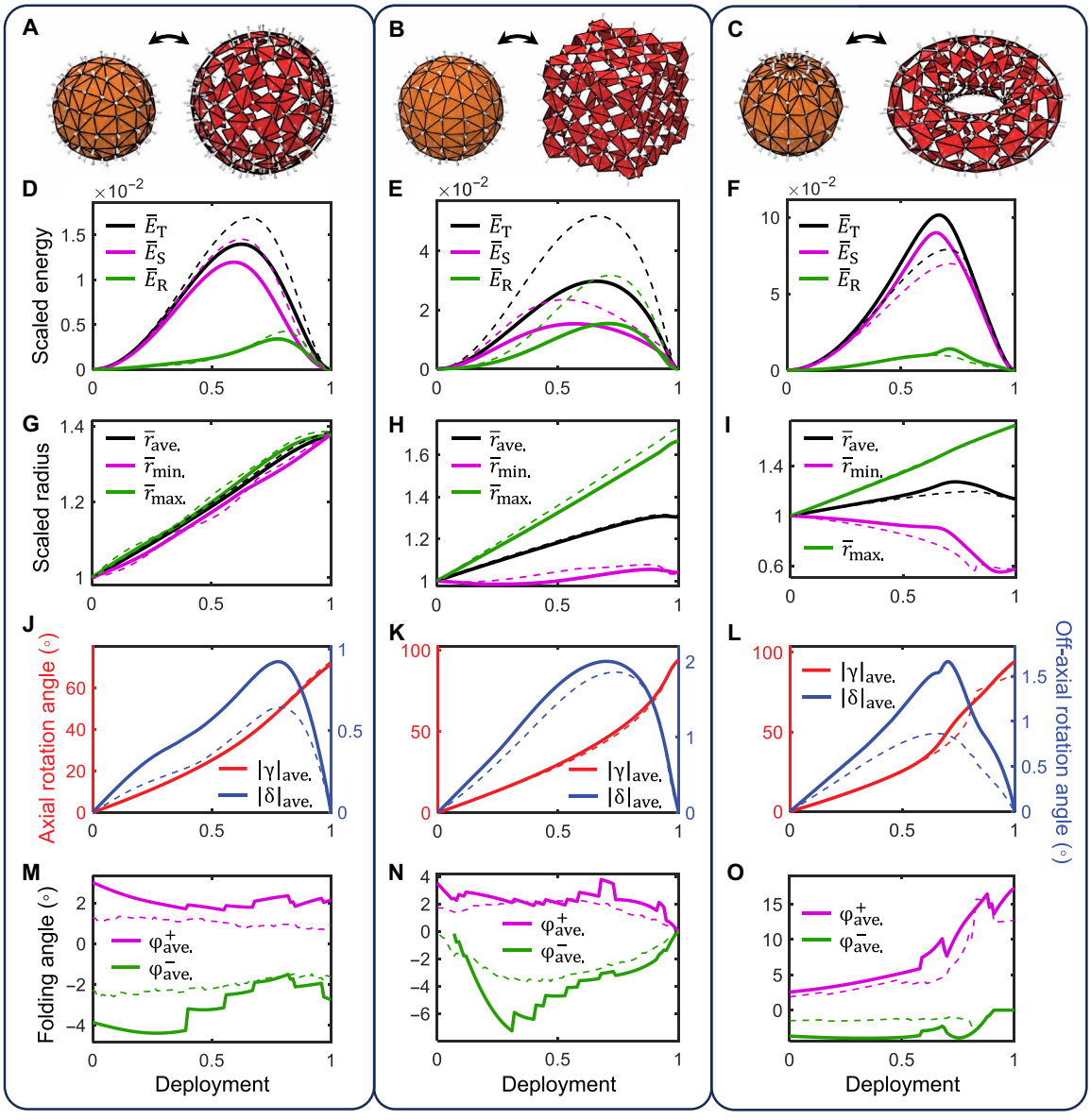

Fig. 3. Energy landscapes and geometric metrics evolving along the deployment path of the bistable ori-kiri assemblages. (**A**) Scaling between two spheres. (**B**) Shape morphing between a compact sphere and a deployed cube. (**C**) Topology morphing between a compact sphere and a deployed torus. (**D** to **F**) Scaled energy landscape: total energy $\bar{E}_T$, stretching energy $\bar{E}_S$, and off-axial-rotation energy $\bar{E}_R$. (**G** to **I**) Scaled radius vector length: average $\bar{r}_{ave.}$, minimum $\bar{r}_{min.}$, and maximum $\bar{r}_{max.}$ of all vertices. (**J** to **L**) Axial-rotation angle $|\gamma|_{ave.}$ and off-axial-rotation angle $|\delta|_{ave.}$, absolute and averaged for all hinges. (**M** to **O**) Positive folding angle $\varphi^+_{ave.}$ and negative folding angle $\varphi^-_{ave.}$, averaged for all creases. Dashed lines represent data from models with increased number of panels, i.e., $6 \times 6 \times 6$ for the left and middle columns and 24×12 for the right column.

Downloaded from https://www.science.org at Princeton University on April 30, 2025

deployed RS mesh, we can design another bistable shape-morphing assemblage that approximate a sphere at the compact state and a cube at the deployed state (Fig. 3B).

Geometric metrics

We now characterize the geometric signature of the ori-kiri assemblage morphing between two zero-energy states. We first iteratively minimize the deformation energy of the bar-and-hinge system on the morphing path. As a result, we can obtain the morphing energy landscape (text S6 and movies S1 and S4) and determine the consecutive configurations in each step. We note that for the compact RS sphere (deployed to sphere or cube), the control nodes are located at the corners of the faces. For the compact UV sphere (deployed to torus), the control nodes are located at the outer circumference of the sphere. Then, with these consecutive configurations, we can calculate specific geometric metrics that describe their deformation, such as the radius vector length, the rotation angle of hinges, and the folding angle of creases. We select three representative examples—scaling between two spheres (Fig. 3A), shape morphing between a sphere and a cube (Fig. 3B), and topology morphing between a sphere and a torus (Fig. 3C)—and compare the variations of their energy landscapes and geometric metrics with respect to the pseudo-time t through the morphing path. We also model assemblages with dissimilar panel numbers; we use solid lines for assemblages of $4 \times 4 \times 6$ panels for scaling and shape morphing and assemblages of 16×8 panels for topology morphing and dash lines for assemblages of $6 \times 6 \times 6$ panels for scaling and shape morphing and assemblages of 24×12 panels for topology morphing.

Energy landscape

From the energy landscapes, we can immediately appraise the bistability of the ori-kiri assemblages, all illustrated with zero energy at their compact ($t = 0$) and deployed states ($t = 1$) and a barrier in the total energy $\overline{E}_T$ to transit from one zero-energy state to another (Fig. 3, D to F). For the sphere-sphere scaling (Fig. 3D) and sphere-torus morphing (Fig. 3F), the stretching energy $\overline{E}_S$ (caused by bar stretching) is much larger than the off-axial-rotation energy $\overline{E}_R$ (caused by the rotation of the panels deviating from the revolute joint axes). In contrast, for the sphere-cube morphing (Fig. 3E), $\overline{E}_R$ is comparable with $\overline{E}_S$. This is attributed to the dramatic curvature change at the cube edges, which increases the rotation energy.

Radius vector length

This metric represents the distance between the vertices and the centroid of the closed surface. We note that the distance is scaled such that its initial value is equal to 1. From the statistics of this metric among all vertices, such as the average $\overline{r}_{ave.}$, the minimum $\overline{r}_{min.}$, and the maximum $\overline{r}_{max}$, we can gain insights into the evolution of distinct features emerging from shape and topology variations. For instance, for the sphere-sphere scaling (Fig. 3G), $\overline{r}_{ave.}$, $\overline{r}_{min.}$, and $\overline{r}_{max.}$ keep almost identical when they increase simultaneously, indicating a uniform expansion of the assemblage. For the sphere-cube morphing (Fig. 3H), the initially identical radius vector lengths diverge to dissimilar values: $\overline{r}_{ave.}$ and $\overline{r}_{max.}$ exhibit increase trends, while $\overline{r}_{min.}$ only varies around a constant value. For the sphere-torus morphing (Fig. 3I), the divergence of $\overline{r}_{ave.}$, $\overline{r}_{ave.}$, and $\overline{r}_{max.}$ is substantial, where $\overline{r}_{max.}$ keeps increasing, while $\overline{r}_{ave.}$ decreases during most of the deployment. This strong divergence reflects the highly non-uniform morphing and is closely associated with the topological change of the assemblage.

Rotation angle of hinge

The relative rotation between two panels at their common vertex reflects the kirigami-motion feature of the ori-kiri assemblages. It can be decomposed into a combination of two successive rotations: the axial rotation around the hinge at the common vertex and the off-axial rotation, if the off-axial-rotation angle is much smaller than π (text S6). To investigate the overall rotation angles in all hinges, we propose two statistics: the average absolute value of the axial rotation angles $|\gamma|_{ave.}$ and the average absolute value of the off-axial-rotation angles $|\delta|_{ave.}$. The absolute operator is used to eliminate the positive and negative signs due to dissimilar rotation directions (counterclockwise or clockwise) and then extract the magnitude of the angles. Among all three morphing cases (Fig. 3, J to L), we can observe comparable variation profiles for both $|\gamma|_{ave.}$ and $|\delta|_{ave.}$. The axial rotation angles $|\gamma|_{ave.}$ exhibit monotonic rising trends from 0 to around 90°, which reflects the deployment process with slit opening and surface area increasing. In contrast, the off-axial-rotation angles $|\delta|_{ave.}$ first increase from 0 to a peak value and then decrease back to 0 at $t = 1$, indicating that the compatibility is broken between two compatible states. During the entire deployment process, $|\gamma|_{ave.}$ maintains low magnitude values below 2°, which is consistent with our assumption of small off-axial-rotation angles in the formulation of off-axial-rotation energy.

Folding angle of crease

In contrast with the rotation angle of hinges, the origami-motion contribution of our ori-kiri assemblages is represented by the folding angle variation between adjacent panels along their common edge. If the two panels are in a common plane, then the folding angle is defined to be zero. We stipulate that the folding angle is in the positive range (0°, 180°] if the crease is a mountain and in the negative range [−180°, 0) if the crease is a valley. We propose two statistics of the folding angles along all the creases, $\varphi^+_{ave.}$, the average value of all the positive folding angles, and $\varphi^-_{ave.}$, the average value of all the negative folding angles. Overall, for the scaling (Fig. 3M) and shape morphing (Fig. 3N), both $\varphi^+_{ave.}$ and $\varphi^-_{ave.}$ vary mostly in the small range of [−5°, 5°]. In contrast, for the topology morphing (Fig. 3O), $\varphi^+_{ave.}$ can reach up to 15°, while $\varphi^-_{ave.}$ maintains small magnitude values below 5°. The large magnitude of $\varphi^+_{ave.}$ indicates the large curvature change between the sphere and the torus. The difference in magnitude between $\varphi^+_{ave.}$ and $\varphi^-_{ave.}$ is caused by the specific crease assignment. As shown in movies S1 and S4, most creases are approximately along the toroidal direction on the deployed toric configurations. Because the curvature in the toroidal direction of the enclosed torus is smaller than the curvature in the poloidal direction, the quadrilateral panels have more chances to bulge outward, which leads to mountain creases and large $\varphi^+_{ave.}$.

Role of number of revolute joints

In the stage II of our design strategy, we introduce revolute joints (1 DOF) to suppress the excessive DOFs arising from spherical joints (3 DOFs) and to achieve global bistability of the ori-kiri assemblages. An interesting question emerges: What is the outcome of partially replacing spherical joints with revolute joints? We discuss the answer and implications of this question with numerical data illustrated in Fig. 4. Specifically, we investigated four morphing cases: the compact and deployed ori-kiri assemblages morph between two spheres (Fig. 4A), a sphere and a cube (Fig. 4B), a cube and a sphere (Fig. 4C), and a sphere and a torus (Fig. 4D). We denote the number of revolute joints by N_r, the number of spherical joints by N_s, and the

Downloaded from https://www.science.org at Princeton University on April 30, 2025

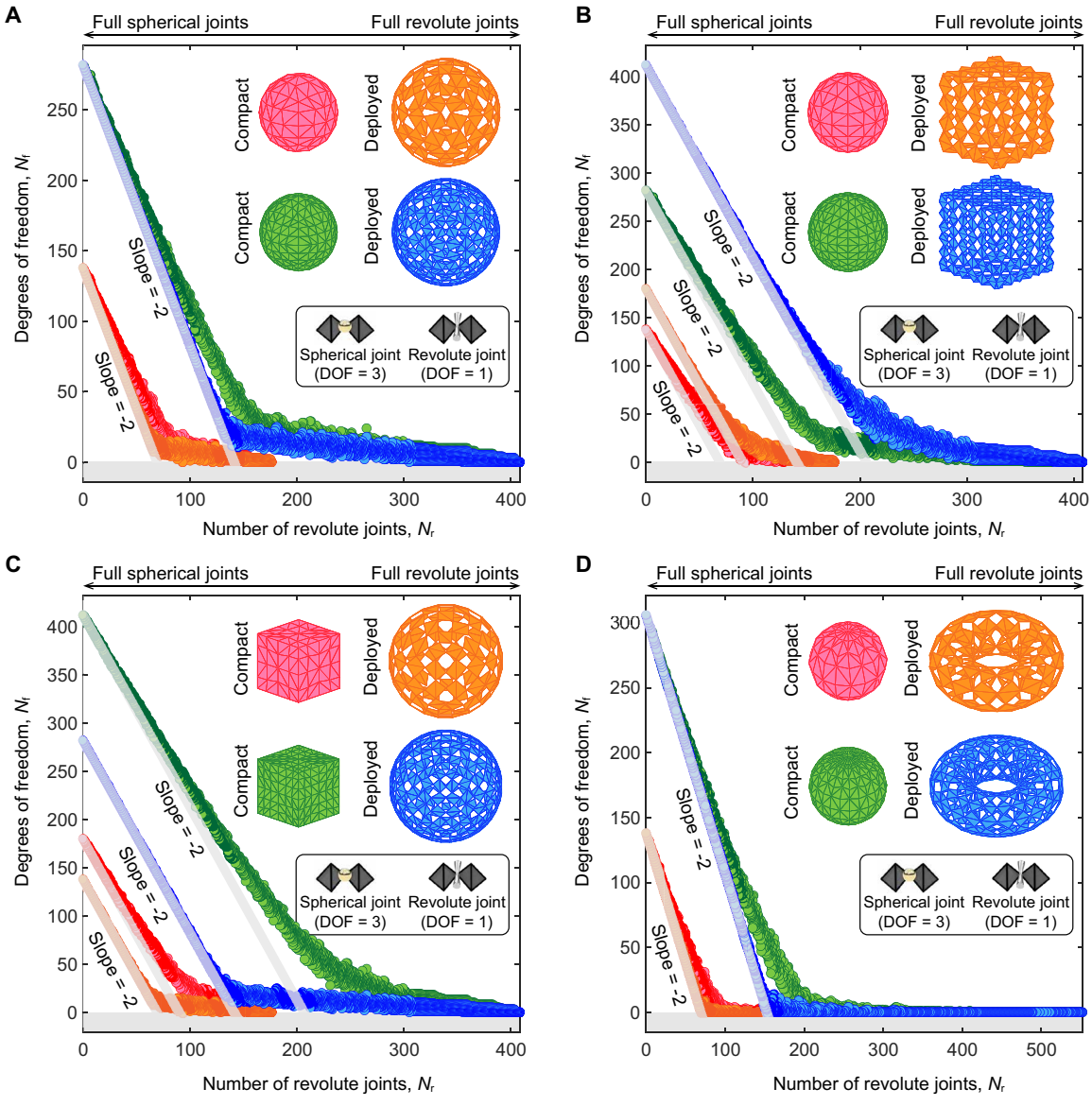

Fig. 4. Relationship between the number of DOFs N_f and the number of revolute joints N_r for the ori-kiri assemblages. For each value of N_r, 10 data points (N_r, N_f) are sampled for randomly assigned locations of revolute joints. The compact and deployed ori-kiri assemblages morph between (**A**) two spheres, (**B**) a sphere and a cube, (**C**) a cube and a sphere, and (**D**) a sphere and a torus. In (A) to (C), the assemblages are composed of $4 \times 4 \times 6$ or $6 \times 6 \times 6$ panels. In (D), the assemblages are composed of 16×8 or 24×12 panels.

total number of joints by N_j, so we have $N_j = N_s + N_r$. If N_r is zero, then all the joints are spherical, whereas, if N_r equals N_j, then all the joints are revolute. Between the bounds, i.e., if $0 < N_r < N_j$, then we have numerous choices for revolute joints among all the N_j joints. Either a distinct value of N_r or a dissimilar assignment of revolute joints can give rise to specific DOFs (denoted by N_f) of these ori-kiri configurations. Only if both the compact and deployed configurations have 0 DOF ($N_f = 0$), then the morphing of an ori-kiri assemblage is globally bistable. To characterize this observation, we randomly assign N_r revolute joints and retain the others as spherical joints, before computing N_f through the method described in text S5. This enables to generate ten data points (N_r, N_f) for each $N_r \in (0, N_j)$. If $N_r = 0$ or N_j, then there is only one way to assign the joints, that is, full spherical joints or full revolute joints; in either case, we can compute N_f as well. Together, we obtain all the data points (the scattered circles) in Fig. 4.

From Fig. 4, first, we can observe that the increase of N_r generally causes the decrease of N_f. The decrease is initially fast if N_f is large and then slows if when N_f approaches zero. We attribute this rate change to the higher probability of introducing redundant kinematic constraints when the total number of constraints (or the number of revolute joints N_r) becomes larger. Second, we can observe that, for a given value of N_r, N_f is generally not determined, varying slightly for different assignments of revolute joints (corresponding to the dissimilar randomly sampled data points). If N_r is sufficiently large, then N_f can be zero although $N_r < N_j$. This implies that a

Downloaded from https://www.science.org at Princeton University on April 30, 2025

partial replacement of spherical joints with revolute joints can preserve the bistability. On the other hand, when N_r closely approaches but not matches N_j, it is still possible that N_f is not zero, for some specific assignments of the revolute joints. This explains why we assign full revolute joints at the second design stage, thereby guaranteeing bistability, i.e., N_f is always zero for $N_r = N_j$.

The existence of redundant constraints can explain some other features of the scatter plots in Fig. 4. First, for the deployed configurations (corresponding to the blue and orange circles), N_f drops with an almost constant slope of −2 at the initial range. In contrast, for the compact configurations (corresponding to the pink and green circles), N_f decreases with varying slopes that are close to −2 but gradually increase. This can be explained by observing that the compact configurations have several overlapping bars. The overlapping may increase the number of redundant kinematic constraints. Second, if all the joints are spherical ($N_r = 0$), then the cubes have more DOFs than the spheres (see Fig. 4, B and C). This can be attributed to the large number of coplanar bars in the cubes, a phenomenon that may increase the number of redundant kinematic constraints.

Global size change upon deployment

For all the morphing cases that are discussed above, we have specified reference opening angles $\omega = 0.5\pi$ for the RS meshes and $\omega = 0.4\pi$ for the UV meshes. By specifying distinct values of ω, we can adjust the global size change of the deployed configurations with respect to the compact size. We illustrate this effect in Fig. 5. Specifically, we calculate the global surface area expansion ratios (denoted by α) of unit spheres that are deployed to spheres, cubes, and tori. These configurations are obtained by solving Eq. 1 with various values of ω between 0.2π and 0.8π. One can see that large α appears at around $\omega = 0.5\pi$, corresponding to large opening slits. On the other hand, α becomes small for $\omega = 0.2\pi$ or 0.8π, corresponding to small opening slits. It is worth noting that, for a given ω, α varies for dissimilar deployed shapes. The cubes or tori tend to have larger α than the deployed spheres do. This can be explained by observing that the deployed cubes or tori are substantially different in shape from the compact spheres, while the deployed spheres only have size change. For a given reference opening angle and prescribed target shape, α is also governed by the number of panels constituting the assemblages. However, this effect is less substantial; the red and blue scatters generally appear in pairs as shown in Fig. 5.

Unitary ori-kiri metamaterials with inner support

To further validate the shape morphing and topology morphing of the proposed ori-kiri design strategy, we extend this concept to unitary structural materials and conduct proof-of-concept validation and finite element simulations. The unitary ori-kiri metamaterials (Fig. 6, A and E) were fabricated using multi-jet fusion (MJF) 3D printing technology with the thermoplastic polyurethane (TPU) powder. Because of the imperfect hinge orientations, the unitary ori-kiri metamaterials lose their intended bistable properties, necessitating auxiliary inner support to achieve their potential functionalities.

We perform finite element simulations (ABAQUS, Dassault Systems) on a representative unit that is $^1/_8$ of the unitary cube or sphere, leveraging their mirror and axial rotational symmetry, respectively. Consistent with the control nodes selected for the truss model simulation (movie S1), the loadings are applied to the living hinges located on the symmetry planes, which exhibit the largest deformation throughout the deployment. Specifically, circular-envelope displacement loadings and reflection-symmetry boundary conditions are applied to these hinges, highlighted in red and yellow, respectively (Fig. 6B). In the unitary sphere model, horizontal outward displacements are applied to the hinges on the neutral plane, vertical inward displacements are applied to the hinges at the polar points, and axial rotational symmetry boundary conditions are imposed on the hinges located on the periodic boundaries (Fig. 6F).

Guided by the strain distribution of the deployed sphere (illustrated in Fig. 6C), we incorporated two inner rigid rings into the cubic specimen, resulting in the deployed unitary sphere (Fig. 6D). From a comparison between the representative symmetric undeformed and deformed units of the sphere model in Fig. 6G, we observe the local snapping of the panels around the poles where stress concentration occurs. Accordingly, we applied an inner rigid ring at

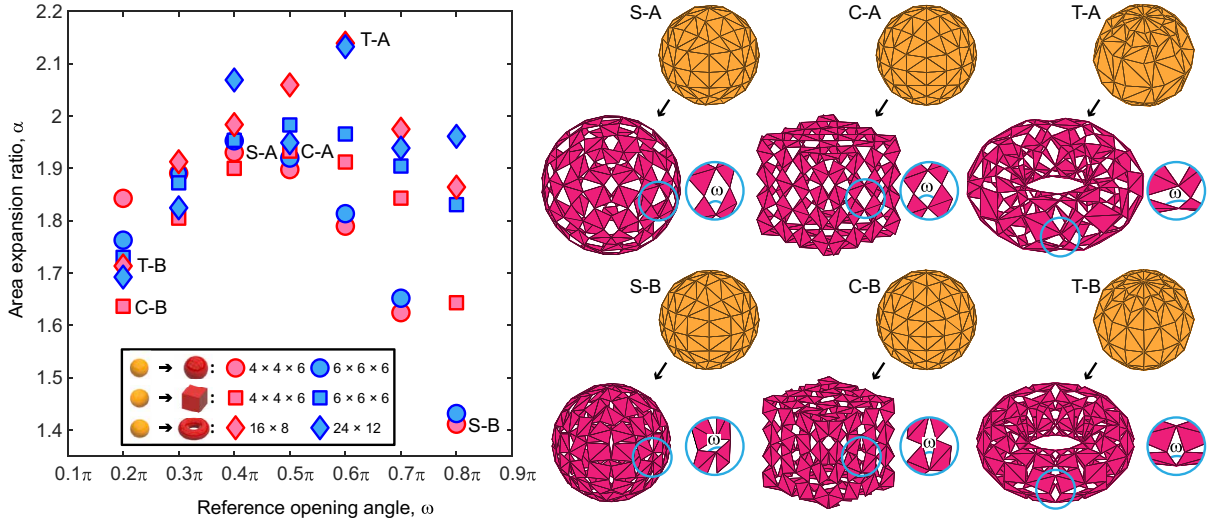

Fig. 5. Global size range of deployed ori-kiri assemblages for a compact unit sphere. The global surface area expansion ratios of the deployed spheres, cubes, and tori are controlled by the target reference opening angle ω varying between 0.2π and 0.8π.

Downloaded from https://www.science.org at Princeton University on April 30, 2025

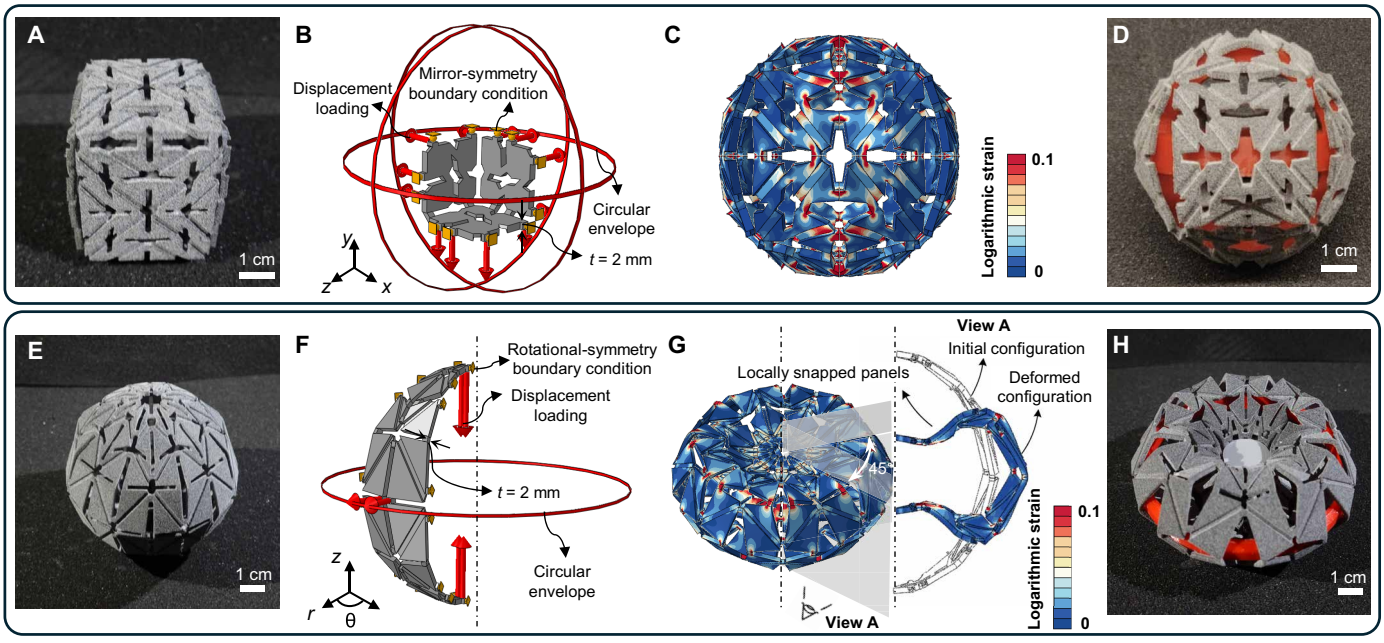

Fig. 6. Shape morphing and topology morphing of unitary ori-kiri metamaterials with inner support. Shape morphing from a cube to a sphere: (**A**) the 3D printed cube; (**B**) loading conditions applied to reduced symmetric unit representing $^1/_8$ of the cube for finite element simulations; (**C**) strain distribution of the deployed sphere; (**D**) the physical deployed sphere with inner support. Topology morphing from a sphere to a torus: (**E**) the 3D printed sphere; (**F**) loading conditions applied to reduced symmetric unit representing $^1/_8$ of the sphere for finite element simulations; (**G**) strain distribution of the deployed torus; (**H**) the physical deployed torus with inner support.

the equator and two additional blockers at the poles of the specimen to achieve the designated deployed torus, as shown in Fig. 6H. Overall, despite the reduced structural bistability compared to their assemblage counterparts, the unitary-piece ori-kiri model, assisted by the inner support, can still show the attainment of a topology change, hence showing promising extensions into the realm of 3D printed metamaterials.

Reprogrammable stiffness and permeability

The shape morphing from a cube into a sphere gives rise to a notable change in curvature and perforation area, thereby empowering the ori-kiri assemblage (Fig. 2G) with distinct stiffness and permeability in its two stable states. In its cubic configuration, the specimen exhibits two primary orientations: one aligned parallel to the discontinuous intersections (green lines, direction 1) and the other perpendicular to them (direction 2), each delivering dissimilar mechanical responses. We examined the directional force-displacement behavior of the specimen in both its two stable states (Fig. 7, A and B), and the corresponding effective compression stiffness (secant slope of the force-displacement curve) and energy dissipation ratio during a loading-unloading cycle are summarized in Fig. 7C.

In its cubic state, the ori-kiri assemblage demonstrates substantially higher effective compression stiffness in both directions 1 and 2, with values ~803 and 504 %, respectively, of those in the spherical state at a compression of 8 mm. This evident variation in stiffness results from the emergence of the global curvature, which shifts the energy distribution of the assemblage from the compression of the constituent panels to the relative out-of-plane bending around each revolute hinge. The effective stiffness of the assemblage in its cubic state exhibits an evident increase (see the red and gray curves in Fig. 7C) as the compressive load raises. This can be attributed to the manufacturing-induced gap between adjacent panels, which is suppressed by the compression, and to the occurrence of self-contact between panels. Although the deployed sphere features a drop of stiffness, the round shape may be advantageous over the cube in isolating low-frequency vibration or mitigating stress concentration. We point out that the anisotropy of the stiffness response in the cubic state becomes more pronounced with increasing compression, while, in the spherical state, the stiffness tends to be more isotropic at relatively large displacements.

The ori-kiri assemblage delivers certain mechanical hysteresis during a loading-unloading cycle due to the frictional rotation of each revolute hinge. Unlike the stiffness response (Fig. 7C, top), the mechanical hysteresis performance, evaluated by the energy dissipation ratio $E_d / (E_d + E_r)$, where E_d is the dissipated energy and E_r is the return energy (inset in Fig. 7C, bottom), shows less dependence on shape or direction (Fig. 7C, bottom). This phenomenon is primarily attributed to the fact that the axial-rotation of individual panels is not a preferred deformation mode of the assemblage under global compression. We point out that the prototype cannot transit between the two stable configurations under the application of uniaxial compression. The instability of the prototype therefore must be triggered through the application of another set of external loadings, as shown in movie S1. Here, we apply displacement boundary conditions at multiple nodes to drive the transition as performed in our numerical simulation. As shown in movie S2, we open and close multiple slits with wires to realize the transition.

During the bistable transition from a cube to a sphere, the surface area covered by the ori-kiri assemblage boosts to 200 % of its initial value, enabling the originally enclosed structure to become permeable. Representative states of the assemblage are depicted in Fig. 7D, showcasing various intermediate configurations that enable

Downloaded from https://www.science.org at Princeton University on April 30, 2025

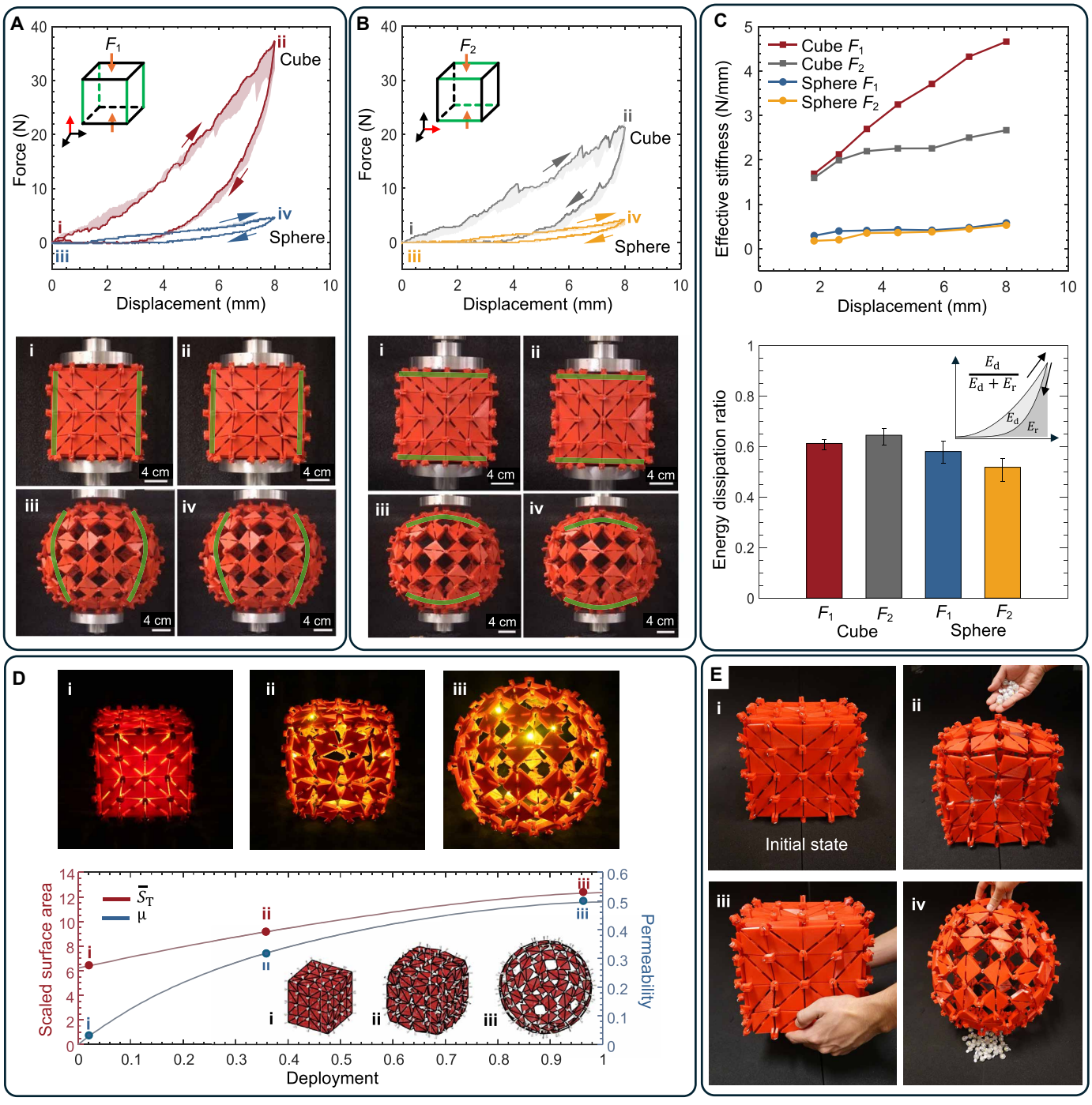

Fig. 7. Reprogrammable stiffness and permeability of the bistable ori-kiri assemblage transitioning from a cube to a sphere. (**A**) Force-displacement response of the assemblage along direction 1; the red curve represents the cubic state, and the blue curve represents the spherical state. (**B**) Compressive response of the assemblage along direction 2; the gray curve represents the cubic state, and the yellow curve represents the spherical state. (**C**) Directional compression stiffness and energy dissipation ratio of the ori-kiri assemblage in its two states. Shaded areas in (A) and (B) and error bars in (C) denote the minimum and maximum of the data from three repeated tests. (**D**) Evolution of the permeability of the ori-kiri assemblage during its bistable shape transformation. (**E**) Packaging application of the ori-kiri assemblage.

Downloaded from https://www.science.org at Princeton University on April 30, 2025

adjustable levels of light illumination. This feature has potential applications across various fields. For example, the ori-kiri assemblage, with panels coated with insulation films, can be harnessed for adaptive shields enabling the control of thermal, fluidic, or electromagnetic flux on demand. Additionally, it can serve as an expandable packaging solution, allowing controllable release of a granular cargo with dissimilar grain sizes at customized rate, as demonstrated in Fig. 7E.

Extension to irregular shapes

We have showed the generality of our two-stage design strategy with two dissimilar meshes used for shape morphing (the RS mesh) and topology morphing (the UV mesh). Here, we show that our strategy is general in an additional aspect; it can accommodate free-form irregular shapes. Figure 8 shows examples of shape-morphing into irregular shapes. The first morphs from a sphere to an egg shape (Fig. 8C), a design obtained by solving the optimization problem given by Eq. 1. The egg shape can be realized by simply modifying the maps $\mathbf{X}_c(\mathbf{P}_c; a_c)$ and $\mathbf{X}_d(\mathbf{P}_d; a_d)$ (see Eqs. 5 and 6) in the compatibility constraint function $f_{comp.}$ (see Eq. 4). For the compact sphere, the map $\mathbf{X}_c(\mathbf{P}_c; a_c)$ becomes

$$(x, y, z) = \mathbf{g}_{\text{sphere}-\text{RS}}(p, q; k, a_c);\ (x, y, z) \in \mathbf{X}_c,\ (p, q) \in \mathbf{P}_c,\ k = 1, 2, \ldots, 6 \tag{14}$$

For the deployed egg shape, the map $\mathbf{X}_d(\mathbf{P}_d; a_d)$ becomes

$$(x, y, z) = (\tilde{x}, \tilde{y}, 1.2\tilde{z} + 0.3\tilde{z}^2),$$
$$(\tilde{x}, \tilde{y}, \tilde{z}) = \mathbf{g}_{\text{sphere}-\text{RS}}(p, q; k, a_d);\ (x, y, z) \in \mathbf{X}_d,\ (p, q) \in \mathbf{P}_d, k = 1, 2, \ldots, 6 \tag{15}$$

The index k denotes the six different faces on the RS meshes. The explicit expression of $\mathbf{g}_{\text{sphere}-\text{RS}}$ is given in text S2. To be consistent with the reduced symmetry of the egg shape, the symmetry constraint function $f_{sym.}$ in Eq. 1 only involves two planes of mirror symmetry for the egg shape. With Eqs. 14 and 15, we can use the regular parametrization (see text S3) to generate the initial geometry for the optimization (see Fig. 8A) and then optimize it to obtain the compatible compact and deployed configurations. This finalizes the first design stage. The second design stage is exactly as before, i.e., we assign the revolute joints to achieve global bistability (see Fig. 8C).

In addition to the egg shape, the other example in Fig. 8D shows the morphing of a sphere into a completely irregular shape with no mirror or rotational symmetry, which we call the "onigiri" shape. In this case, the map $\mathbf{X}_c(\mathbf{P}_c; a_c)$ is still expressed by Eq. 14, while the map $\mathbf{X}_d(\mathbf{P}_d; a_d)$ is given by

$$(x, y, z) = (\tilde{x} + 0.25\tilde{x}^2, \tilde{y} + 0.25\tilde{y}^2, \tilde{z} + 0.25\tilde{z}^2),$$
$$(\tilde{x}, \tilde{y}, \tilde{z}) = \mathbf{g}_{\text{sphere}-\text{RS}}(p, q; k, a_d);\ (x, y, z) \in \mathbf{X}_d,\ (p, q) \in \mathbf{P}_d, k = 1, 2, \ldots, 6 \tag{16}$$

The symmetry constraint function $f_{sym.}$ in Eq. 1 is removed for the irregular onigiri shape. Again, we use the regular parametrization (see text S3) to generate the initial geometry for the optimization (see Fig. 8B) and then optimize it to obtain the compatible compact and deployed configurations. We then assign the revolute joints to finalize the bistable assemblage (see Fig. 8D).

We perform the numerical energy analysis (text S6) and illustrate the results in Fig. 8E for the egg shape and in Fig. 8I for the onigiri shape. Compared to the energy curves for scaling a sphere (see Fig. 3, A and D), the energy landscapes for the irregular egg and onigiri shapes exhibit sharp peaks and higher peak energy (which is nondimensionalized), indicating higher incompatibility on their morphing paths. Moreover, for the onigiri shape, local non-smoothness is observed, reflecting the local instabilities due to the large size and shape discrepancy of the individual cells. The consecutive configurations on the deployment paths of the egg and onigiri shapes are provided in movie S5. We also illustrate the geometric metrics evolving along the deployment path of the egg (Fig. 8, F to H) and onigiri shapes (Fig. 8, J to L). The morphing from the sphere to irregular shapes causes a divergence of the radius vector lengths (Fig. 8, F and J). The larger off-axial-rotation angles, peak values around 3° as shown in Fig. 8 (G and K) versus peak value less than 1° as shown in Fig. 3J, indicates the higher incompatibility on their morphing paths of the irregular shapes. The local sharp change of the irregular shapes induces large magnitude of the folding angles (around −7° in Fig. 8H and around −9° in Fig. 8L).

DISCUSSION

This work has presented a class of ori-kiri assemblages that can morph between two stable configurations approximating different closed surfaces. A two-stage design framework is introduced to generate the crease-slit patterns of the ori-kiri assemblages. The framework involves first applying a hybrid origami-kirigami principle to meet the geometric compatibility condition, followed by incorporating kinematic constraints to ensure that the system is kinematically determinate.

Surface morphing generally involves a combination of bending and stretching of the constituent elements in a discrete surface or the continuous medium of a unitary surface, resulting in changes to both curvature and area. Relying solely on either origami or kirigami principles poses challenges in achieving specific target shapes, particularly closed surfaces. To address this issue, we have chosen to integrate origami and kirigami principles, enabling the morphing of complex shapes and even topologies. Furthermore, integrating origami and kirigami principles substantially increases the DOFs in the system, resulting in a floppy and unstable mechanism. To mitigate this, we selectively restrict the rotational DOFs at the hinges, allowing adjacent panels to rotate exclusively around a designated axis. This strategy provides the ori-kiri assemblages with structural rigidity and deployment guidance.

Governed by a combination of distinct crease-dominated and slit-dominated deformation modes, diverse types of closed-surface morphing are demonstrated including scaling, shape morphing, and topology morphing. Our design framework is intentionally conceived to separate geometry considerations from mechanics considerations, hence constituting a two-stage process: Only if the geometry satisfies compatibility at the first design stage, we can use this geometry in the second design stage to calculate the direction of the revolute joints. The first design stage is thus purely based on geometry, as no constraints are applied to the vertices that connect the panels; this implies that the nodes are essentially spherical joints. Only at the second design stage do we tackle the mechanics by introducing revolute joints that reduce the DOFs to zero. By doing so, we obtain the bistable assemblages. If the first design stage involves another optimization target, for example, minimizing the number of revolute joints to induce bistability, then the revolute joints should be applied in the first design stage. In other words, the two design stages must be integrated into one process. In this case, we

Downloaded from https://www.science.org at Princeton University on April 30, 2025

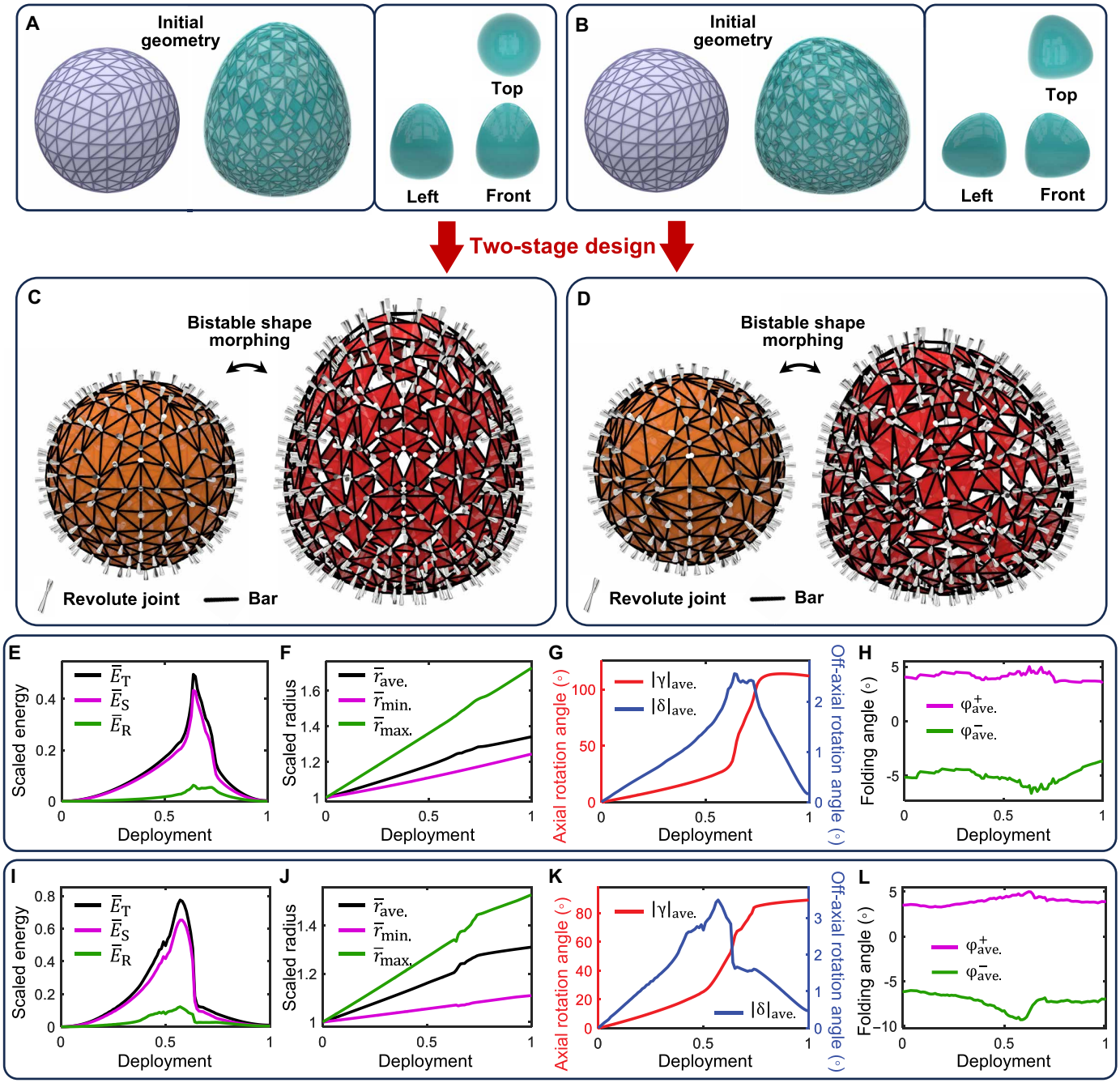

Fig. 8. Design of irregular shape-morphing bistable ori-kiri assemblages and their energy landscapes and geometric metrics evolving along the deployment path. (**A** and **B**) Initial geometry and (**C** and **D**) the compact and deployed bistable ori-kiri assemblages of the morphing egg [(A) and (C)] and the morphing onigiri [(B) and (D)]. (**E** to **L**) Energy landscapes and geometric metrics of the morphing egg [(E) to (H)] and the morphing onigiri [(I) to (L)]: Energy landscape: total energy $\bar{E}_T$, stretching energy $\bar{E}_S$, and off-axial-rotation energy $\bar{E}_R$ [(E) and (I)]; radius vector length: average $\bar{r}_{ave.}$, minimum $\bar{r}_{min.}$, and maximum $\bar{r}_{max.}$ of all vertices [(F) and (J)]; axial-rotation angle $|\gamma|_{ave.}$ and off-axial-rotation angle $|\delta|_{ave.}$, absolute and averaged for all hinges [(G) and (K)]; positive folding angle $\varphi^{+}_{ave.}$ and negative folding angle $\varphi^{-}_{ave.}$, averaged for all creases [(H) and (L)].

anticipate that the integrated process will inevitably increase the complexity of the formulation and the attainment of the solution.

We simulate the morphing process with a truss surrogate model and obtain energy landscapes that validate the bistability pursued by our proposed design framework. A set of prototypes are fabricated to show the attainment of shape morphing between a cube and a sphere and the topology morphing between a sphere and a torus. With the cube-sphere assemblage, we show its programmable stiffness and permeability and enlighten potential applications, including transportable packaging and electromagnetic shielding.

The platform here presented, leveraging a fine synergism between origami and kirigami principles, provides a promising avenue for morphing closed surfaces. For the shape morphing, our approach effectively stitches together six separate continuous meshes. This strategy may

Downloaded from https://www.science.org at Princeton University on April 30, 2025

be further extended by increasing the number of separate meshes and optimizing the way that they are stitched together (i.e., determining the connection between adjacent meshes) to morph target surface of higher complexity. While the single mesh enables topology morphing between a sphere and a torus, stitching multiple meshes may enable more complex topology transformations. Moreover, the adaptability of our framework may be enhanced by adopting a triangular (kagome) kirigami pattern, which offers more DOFs than quadrilateral meshes to fit complex surfaces (*28*), or a hybrid of quadrilateral and triangular patterns to pursue a balance between design flexibility and structural stability.

Last, the principle of integrating origami and kirigami is not limited to designing mechanism assemblages, as we qualitatively touch upon the more challenging problem of morphing 3D printed metamaterials. We fabricate ori-kiri metamaterials with features of shape morphing and topology morphing and acknowledge the current fabrication-driven challenge of realizing carefully oriented spatial hinges, hence only partially demonstrating the achievement of bistability. Morphing bistable closed surfaces through a set of unitary-piece metamaterials across various scales is the subject of future study, harnessing more powerful fabrication technology.

MATERIALS AND METHODS

Fabrication

Panels of the ori-kiri assemblage in Figs. 2G and 7 were made of polylactic acid filament and water-dissolvent support material polyvinyl alcohol filament with a dual-extruder fused deposition modeling 3D printer (QIDI TECH i-fast 3D printer, Wenzhou, Zhejiang, China) by 0.4-mm line width, 0.2-mm layer height, 15% infill density of gyroid pattern, and 60 mm/s printing speed. Panels of the ori-kiri assemblage in Fig. 2H were made of Nylon PA12 with an SLS (selective laser sintering) 3D printer by 0.8-mm wall thickness. Each panel was carefully designed with orientated revolute hinges such that it can be connected to its adjacent panels via pin joints. The unitary models in Fig. 6 were made of TPU powder with an MJF 3D printer.

Experiments

The quasi-static compression tests of the ori-kiri assemblage in Fig. 7 were performed on the Electro-Force 3510 fatigue machine (Bose Corporation, Framingham, Massachusetts) with a loading rate of 0.16 mm/s. The tests were repeated three times in each direction and each state for the experimental uncertainty regime.

Supplementary Materials

The PDF file includes:
Supplementary Text
Figs. S1 to S17
Legends for movies S1 to S5

Other Supplementary Material for this manuscript includes the following:
Movies S1 to S5

REFERENCES AND NOTES

1. K. Bertoldi, V. Vitelli, J. Christensen, M. Van Hecke, Flexible mechanical metamaterials. *Nat. Rev. Mater.* **2**, 17066 (2017).
2. X. Liu, M. Gao, J. Chen, S. Guo, W. Zhu, L. Bai, W. Zhai, H. Du, H. Wu, C. Yan, Y. Shi, J. Gu, H. J. Qi, K. Zhou, Recent advances in stimuli-responsive shape-morphing hydrogels. *Adv. Funct. Mater.* **32**, 2203323 (2022).
3. A. Sellitto, A. Riccio, Overview and future advanced engineering applications for morphing surfaces by shape memory alloy materials. *Materials* **12**, 708 (2019).
4. L. K. Rivera-Tarazona, V. D. Bhat, H. Kim, Z. T. Campbell, T. H. Ware, Shape-morphing living composites. *Sci. Adv.* **6**, eaax8582 (2020).
5. S. W. Ula, N. A. Traugutt, R. H. Volpe, R. R. Patel, K. Yu, C. M. Yakacki, Liquid crystal elastomers: An introduction and review of emerging technologies. *Liquid Cryst. Rev.* **6**, 78–107 (2018).
6. E. Hajiesmaili, N. M. Larson, J. A. Lewis, D. R. Clarke, Programmed shape-morphing into complex target shapes using architected dielectric elastomer actuators. *Sci. Adv.* **8**, eabn9198 (2022).
7. X. Ning, X. Wang, Y. Zhang, X. Yu, D. Choi, N. Zheng, D. S. Kim, Y. Huang, Y. Zhang, J. A. Rogers, Assembly of advanced materials into 3D functional structures by methods inspired by origami and kirigami: A review. *Adv. Mater. Interfaces* **5**, 1800284 (2018).
8. J. W. Boley, W. M. van Rees, C. Lissandrello, M. N. Horenstein, R. L. Truby, A. Kotikian, J. A. Lewis, L. Mahadevan, Shape-shifting structured lattices via multimaterial 4D printing. *Proc. Natl. Acad. Sci. U.S.A.* **116**, 20856–20862 (2019).
9. D. Hwang, E. J. Barron, A. B. M. T. Haque, M. D. Bartlett, Shape morphing mechanical metamaterials through reversible plasticity. *Sci. Robot.* **7**, eabg2171 (2022).
10. L. Jin, M. Yeager, Y.-J. Lee, D. J. O'Brien, S. Yang, Shape-morphing into 3D curved surfaces with nacre-like composite architectures. *Sci. Robot.* **8**, eabq3248 (2022).
11. S. An, Y. Cao, H. Jiang, A mechanically robust and facile shape morphing using tensile-induced buckling. *Sci. Robot.* **10**, eado8431 (2024).
12. E. Siéfert, E. Reyssat, J. Bico, B. Roman, Bio-inspired pneumatic shape-morphing elastomers. *Nat. Mater.* **18**, 24–28 (2019).
13. K. Liu, F. Hacker, C. Daraio, Robotic surfaces with reversible, spatiotemporal control for shape morphing and object manipulation. *Sci. Robot.* **6**, eabf5116 (2021).
14. C. Jiang, F. Rist, H. Wang, J. Wallner, H. Pottmann, Shape-morphing mechanical metamaterials. *Comput Aided Des.* **143**, 103146 (2022).
15. A. M. Abdullah, X. Li, P. V. Braun, J. A. Rogers, K. J. Hsia, Kirigami-inspired self-assembly of 3D structures. *Adv. Funct. Mater.* **30**, 1909888 (2020).
16. J. S. Birman, J. Eisner, "Surface topolgy" in *Seifert and Threlfall: A Textbook of Topology* (Elsevier, 1980), chap. 6, pp. 134–153.
17. J. R. Weeks, *The Shape of Space* (CRC Press) (2001).
18. B. S. Guru, H. R. Hiziroglu, *Electromagnetic Field Theory Fundamentals* (Cambridge Univ. Press, ed. 2, 2004).
19. F. Beer, E. Johnston, J. DeWolf, *Mechanics of Materials* (McGraw Hill, ed. 4, 2006), chap. 6, pp. 390–413.
20. A. M. Vargason, A. C. Anselmo, S. Mitragotri, The evolution of commercial drug delivery technologies. *Nat. Biomed. Eng.* **5**, 951–967 (2021).
21. C. Liang, Z. Gu, Y. Zhang, Z. Ma, H. Qiu, J. Gu, Structural design strategies of polymer matrix composites for electromagnetic interference shielding: A review. *Nano Micro Lett.* **13**, 181 (2021).
22. M. Pontin, D. D. Damian, Multimodal soft valve enables physical responsiveness for preemptive resilience of soft robots. *Sci Robot.* **9**, eadk9978 (2024).
23. S. J. Callens, A. A. Zadpoor, From flat sheets to curved geometries: Origami and kirigami approaches. *Mater. Today* **21**, 241–264 (2018).
24. C. Ai, Y. Chen, L. Xu, H. Li, C. Liu, F. Shang, Q. Xia, S. Zhang, Current development on origami/kirigami-inspired structure of creased patterns toward robotics. *Adv. Eng. Mater.* **23**, 2100473 (2021).
25. Z. Zhai, L. Wu, H. Jiang, Mechanical metamaterials based on origami and kirigami. *Appl. Phys. Rev.* **8**, 041319 (2021).
26. X. Dang, F. Feng, H. Duan, J. Wang, Theorem on the compatibility of spherical kirigami tessellations. *Phys. Rev. Lett.* **128**, 035501 (2022).
27. L. H. Dudte, E. Vouga, T. Tachi, L. Mahadevan, Programming curvature using origami tessellations. *Nat. Mater.* **15**, 583–588 (2016).
28. G. P. Choi, L. H. Dudte, L. Mahadevan, Programming shape using kirigami tessellations. *Nat. Mater.* **18**, 999–1004 (2019).
29. N. Villanueva, "UV mapping" in *Beginning 3D Game Assets Development Pipeline* (Apress, 2022), chap. 5, pp. 117–149.

Acknowledgments

Funding: D.P. acknowledges the financial support of the Canada Research Chairs Program (257679) and the Natural Sciences and Engineering Research Council of Canada (208241). L.W. acknowledges financial support from the China Scholarship Council (202006280037). S.C. acknowledges financial support from the China Scholarship Council (202206020073). **Author contributions:** Conceptualization: X.D. and D.P. Methodology: X.D., L.W., and D.P. Investigation: X.D., S.C., and A.E.A. Visualization: X.D., S.C., A.E.A., and L.W. Writing—original draft: X.D., S.C., and L.W. Writing—review and editing: X.D., S.C., A.E.A., L.W., and D.P. Supervision: D.P. **Competing interests:** The authors declare that they have no competing interests. **Data and materials availability:** All data needed to evaluate the conclusions in the paper are present in the paper and/or the Supplementary Materials.

Submitted 20 August 2024
Accepted 25 March 2025
Published 30 April 2025
10.1126/sciadv.ads5659

Downloaded from https://www.science.org at Princeton University on April 30, 2025